Calculation of Electron Transfer Rate Constants from Emission Spectra in Re(I) Chromophore−Quencher Complexes

Juan Pablo Claude,[†] Kristin M. Omberg,[‡] Darryl S. Williams,[§] and Thomas J. Meyer*

Department of Chemistry, CB# 3290, University of North Carolina, Chapel Hill, North Carolina 27599-3290 and Office of the Associate Director for Strategic Research, Mail Stop A127, Los Alamos National Laboratory, Los Alamos, New Mexico 87545

Received: May 15, 2002

The photophysical properties of the chromophore−quencher complexes, *fac*-[(4,4′-R_2bpy)$Re^{I}(CO)_3$(LA)]$^{n+}$ (4,4′-R_2bpy = 4,4′-R_2-2,2′-bipyridine, R = Me or ^{t}Bu, and LA = the quinone acceptor ligands, benz[*g*]-isoquinoline-5,10-dione (BIQD), 2-oxy-1,4-naphthoquinone anion (ONQ^-), 1/2 2,6-dihydroxyanthraquinone dianion (AFA^{2-}), or the pyridinium acceptor, 1-methyl-6-oxyquinoline (OQD)) in 1,2-dichloroethane are described. Following Re^{I} → 4,4′-R_2bpy metal-to-ligand charge transfer (MLCT) excitation, intramolecular electron transfer leads to the transients, *fac*-[(4,4′-R_2bpy)$Re^{II}(CO)_3(LA^{\bullet-})]^{n+}$. They have been characterized by emission spectral fitting and transient absorption measurements and, for LA = OQD, by transient infrared measurements. As shown by analysis of excited-state emission, there is weak-to-moderate electronic coupling between the electron donor and acceptor sites in the transients with H_{DA} varying from 153 cm^{-1} for the BIQD complex to 3.9 cm^{-1} for the OQD complex. The transients are redox-separated (RS) states with the electronic configurations $d\pi^5\pi_{LA}{}^{*1}$ for BIQD or $\sigma(Re-O)^1\pi_{LA}{}^{*1}$ for ONQ^-, AFA^{2-}, and OQD. They are weak emitters and return to the ground state largely by nonradiative decay which occurs by back electron transfer (k_{ET}). Reasonable agreement has been reached between k_{ET} and values calculated from kinetic parameters derived by emission spectral fitting and excited-state decay. The RS states for the AFA^{2-} and OQD complexes are remarkably long-lived (τ = 4 μs for LA = AFA^{2-} in DCE at 296 K and 16 μs for LA = OQD in DCE at 296 K) due to orbital and spin restrictions on back electron transfer.

Introduction

In the study of electron transfer, energy transfer, and nonradiative decay, an important development has been the recognition of the close relationship between spectroscopy and reaction dynamics.[1−13] Theoretical expressions have been derived which relate rate constants to molecular quantities such as reorganizational energies, driving forces, and the coupling matrix elements that mix states, all of which can be measured in favorable cases. The application of these ideas has led to the use of emission, absorption, and resonance Raman spectra[14] to evaluate reaction barriers and rate constants for electron and energy transfer in the normal and inverted regions, and for nonradiative decay.[15−29]

This approach requires evaluation of the solvent reorganizational energy, the quantum spacings and changes in equilibrium displacements for the coupled vibrations, and the interaction energy arising from electronic coupling. The first two can be evaluated from absorption and/or emission band shapes and the latter from oscillator strengths by integrating absorption bands, or by evaluating the Einstein coefficient for spontaneous emission by emission quantum yield and lifetime measurements.

Chromophore−quencher complexes, which are molecular assemblies in which electron transfer donor and/or acceptor groups are chemically linked to a chromophore unit, have been useful in these studies. Porphyrin-based chromophores linked to carotenoids[30,31] and anilines[32−34] as donors and quinones as acceptors have been studied extensively, as have chromophore−quencher complexes based on polypyridyl complexes of Ru(II), Os(II), or Re(I), which serve as metal-to-ligand charge transfer (MLCT) chromophores.[35−41] A variety of donors and acceptors have been used in MLCT-based assemblies, including quinones.[42−45] Quinones are attractive as acceptors because they are available in a range of redox potentials by making substituent changes. They are also important components in natural photosynthetic reaction centers.[46]

In this manuscript, we report the photophysical properties of the series of chromophore−quencher complexes, *fac*-[(4,4′-R_2-bpy)$Re^{I}(CO)_3$(LA)]$^{n+}$ (4,4′-R_2bpy = 4,4′-R_2-2,2′-bipyridine, R = Me or ^{t}Bu, and LA = the quinone acceptor ligands, benz-[*g*]isoquinoline-5,10-dione (BIQD), 2-oxy-1,4-naphthoquinone anion (ONQ^-), 1/2 2,6-dihydroxyanthraquinone dianion (AFA^{2-}), or the pyridinium acceptor, 1-methyl-6-oxyquinoline (OQD)). The structures of the ligands and of the complex *fac*-[(4,4′-Me_2bpy)$Re^{I}(CO)_3$(BIQD)]$^+$ are illustrated below.

These complexes were designed to study the relationship between electron transfer and spectroscopy. Given the nature of the chemical links between units, electronic coupling between the metal and acceptor ligand is expected to be moderate for BIQD and weak for the aryloxide ligands. Following Re^{I} → 4,4′-R_2bpy excitation and 4,4′-R_2bpy → LA electron transfer to give *fac*-[(4,4′-R_2bpy)$Re^{II}(CO)_3(LA^{\bullet-})]^{n+}$, $LA^{\bullet-}$ → Re^{II} back electron transfer occurs and can be time-resolved by transient absorption measurements because the one-electron-reduced

* To whom correspondence should be addressed.
[†] Current address: Department of Chemistry, University of Alabama at Birmingham, Birmingham, AL 35294-1240.
[‡] Current address: Systems Engineering & Integration Group, Decision Applications Division, Mail Stop F607, Los Alamos National Laboratory, Los Alamos, NM 87545.
[§] Current address: Research & Development, Texas Eastman Division, Eastman Chemical Company, P.O. Box 7444, Longview, TX 75607-7444.

10.1021/jp021216l CCC: $22.00
Published on Web 08/07/2002

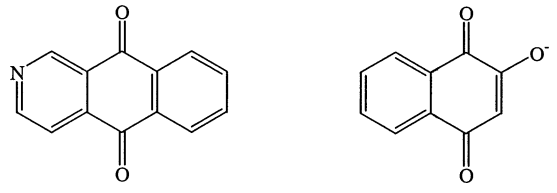

BIQD **ONQ$^-$**

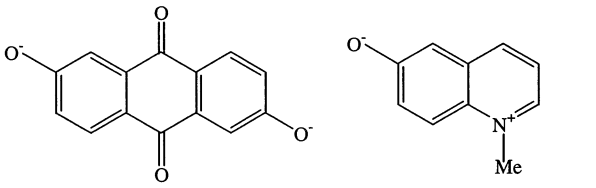

AFA^{2-} **OQD**

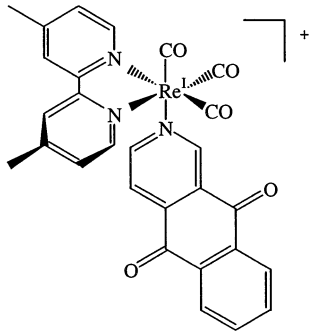

***fac*-[(4,4'-Me$_2$bpy)Re(CO)$_3$(BIQD)]$^+$**

quinone and pyridinium ligands have characteristic absorption features in the near-UV and visible. Most importantly, all of these complexes emit, and analysis of the emission gives the parameters required to calculate both the electron-transfer barrier and electron-transfer coupling matrix elements.[20−23] A preliminary account of this work has appeared.[47]

Experimental Section

Materials. Benz[*g*]isoquinoline-5,10-dione, 2-hydroxy-1,4-naphthoquinone, 2,6-dihydroxyanthraquinone, 6-hydroxyquinoline, 4,4′-dimethyl-2,2′-bipyridine, tetrabutyl-*n*-ammonium hydroxide (1 M solution in H_2O), ammonium hexafluorophosphate, silver triflate, and phenol were purchased from Aldrich and used as received. $Re(CO)_5Cl$ was obtained from Pressure Chemicals and methyl iodide from Fisher. The ligand 4,4′-*tert*-butyl-2,2′-bipyridine[48] and the complexes *fac*-[(4,4′-Me_2bpy)$Re(CO)_3$(OTf)] (bpy = 2,2′-bipyridine; OTf = CF_3SO_3-), *fac*-[(bpy)$Re(CO)_3$(4-Etpy)](PF_6) (4-Etpy = 4-ethylpyridine), and *fac*-[(4,4′-Me_2bpy)$Re(CO)_3$(4-Etpy)](PF_6) were prepared according to literature procedures.[49,50] HPLC grade 1,2-dichloroethane (DCE) was purchased from Aldrich, dried over CaH_2, and distilled under an inert atmosphere before use. All other solvents were reagent grade and used as received.

General Methods. ^{1}H NMR spectra were acquired on Bruker AML300 or WM250 spectrometers, and chemical shifts are reported as ppm vs TMS at 20 °C in CD_2Cl_2 unless otherwise specified. Deuterated solvents were purchased from Cambridge Isotope Labs and used as received. FTIR spectra were collected in KBr disks on a Mattson Galaxy 5020 spectrometer. UV−vis spectra were recorded on an OLIS-modified Cary 14 spectrophotometer in 1-cm path length quartz cuvettes. Analyses were performed by Oneida Research Services.

Syntheses. *fac-[(4,4′-^{t}Bu$_2$bpy)Re(CO)$_3$Cl]*. $Re(CO)_5Cl$ (2.00 g, 5.53 mmol) was slurried in toluene (50 mL) with 4,4′-^{t}Bu$_2$-bpy (1.48 g, 5.53 mmol) and heated at reflux under nitrogen for 1 h. The resulting yellow solution was cooled to room temperature and filtered. The yellow precipitate was washed with diethyl ether and dried to yield 2.8 g (88%) of pure *fac*-[(4,4′-^{t}Bu$_2$bpy)$Re(CO)_3Cl$]. ^{1}H NMR (CD_2Cl_2, ppm): δ 8.92 (d, 2H), δ 8.10 (d, 2H), δ 7.51 (dd, 2H), δ 1.43 (s, 18H).

fac-[(4,4′-^{t}Bu$_2$bpy)Re(CO)$_3$(OTf)]. AgOTf (470 mg, 1.83 mmol) was added to a THF (20 mL) solution of *fac*-[(4,4′-^{t}Bu$_2$bpy)$Re(CO)_3Cl$] (1.00 g, 1.742 mmol). The solution was stirred for 2 h, and the white precipitate of silver chloride was removed by filtration through a pad of Celite. The precipitate was washed with diethyl ether, the solution volume was doubled with hexane and half of the solvent volume was removed under vacuum. The resulting precipitate was filtered, washed with hexane, and dried to yield 1.10 g (91%) of a lemon yellow powder. ^{1}H NMR (CD_2Cl_2, ppm): δ 8.97 (d, 2H), δ 8.09 (d, 2H), δ 7.59 (dd, 2H), δ 1.45 (s, 18H).

fac-[(4,4′-^{t}Bu$_2$bpy)Re(CO)$_3$(OPh)]. A solution containing *fac*-[(4,4′-^{t}Bu$_2$bpy)$Re(CO)_3$(OTf)] (100 mg, 0.14 mmol) and phenol (14 mg, 0.14 mmol) in CH_2Cl_2 (20 mL) was stirred over powdered K_2CO_3 for 24 h. The solution color changed from pale yellow to red-orange over the course of the reaction. The solution was filtered and concentrated under vacuum. Dissolution of the residue in a minimum amount of CH_2Cl_2 and vapor diffusion of diethyl ether into this solution yielded 75 mg (82%) of product as orange needles. ^{1}H NMR (CD_2Cl_2, ppm): δ 8.86 (d, 2H), δ 8.15 (d, 2H), δ 7.49 (dd, 2H), δ 6.87 (dd, 1H), δ 6.36 (t, 1H), δ 6.24 (dd, 2H), δ 1.45 (s, 18H). Anal. Calcd. for $C_{27}H_{29}N_2O_4Re$: C, 51.33%; H, 4.63%; N, 4.43%. Found: C, 51.03%; H, 4.52%; N, 4.40%.

fac-[(4,4′-^{t}Bu$_2$bpy)Re(CO)$_3$(ONQ)]. A solution containing *fac*-[(4,4′-^{t}Bu$_2$bpy)$Re(CO)_3$(OTf)] (100 mg, 0.14 mmol) and 2-hydroxy-1,4-naphthoquinone (25 mg, 0.14 mmol) in CH_2Cl_2 (20 mL) was stirred for 30 min. Powdered K_2CO_3 was added and stirring continued for 24 h. The solution color changed from pale yellow to red over the course of the reaction. The solution was filtered and concentrated under vacuum. Dissolution of the residue in a minimum amount of CH_2Cl_2 and vapor diffusion of diethyl ether into this solution yielded 88 mg (85%) of cherry red needles. ^{1}H NMR (CD_2Cl_2, ppm): δ 8.91 (d, 2H), δ 8.11 (d, 2H), δ 7.97 (dd, 1H), δ 7.73 (dd, 1H), δ 7.6−7.4 (m, 4H), δ 6.03 (s, 1H), δ 1.43 (s, 18H). Anal. Calcd. for $C_{31}H_{29}N_2O_6Re$: C, 52.31%; H, 4.11%; N, 3.94%. Found: C, 52.63%; H, 4.34%; N, 3.44%.

fac-[(4,4′-Me$_2$bpy)Re(CO)$_3$]$_2$(AFA). The conjugated base of anthraflavic acid (2,6-dihydroxyanthraquinone dianion) was prepared by dissolving the compound in a minimum volume of 50% (v:v) THF:MeOH and adding 2 equiv of [(^{n}Bu)$_4$N](OH) (1 M solution in H_2O). The deep red salt [(^{n}Bu)$_4$N](AFA) rapidly precipitated and was collected by filtration. A solution of the AFA salt (240 mg, 0.33 mmol) in 50 mL of 50% (v:v) THF:MeOH was slowly added to a solution of *fac*-[(4,4′-Me_2bpy)-$Re(CO)_3$(OTf)] (100 mg, 0.17 mmol) in 30 mL of the same solvent mixture, resulting in the slow, quantitative precipitation of the orange product. Because this compound is sparingly soluble, no ^{1}H NMR data are available. Anal. Calcd. for $C_{44}H_{30}N_4O_{10}Re_2$: C, 46.07%; H, 2.64%; N, 4.88%. Found: C, 45.52%; H, 2.75%; N, 4.50%.

fac-[(4,4′-^{t}Bu$_2$bpy)Re(CO)$_3$(OQD)](OTf). 6-Hydroxyquinoline was methylated with methyl iodide and deprotonated with [(^{n}Bu)$_4$N](OH) in THF, resulting in precipitation of the zwitterion. A solution of *fac*-[(4,4′-^{t}Bu$_2$bpy)$Re(CO)_3$(OTf)] (100 mg,

0.14 mmol) and 1-methyl-6-oxyquinoline (zwitterion) (23 mg, 0.14 mmol) in CH_2Cl_2 (15 mL) was stirred for 12 h. The solution color changed from pale yellow to pale orange over the course of the reaction. The solution was filtered and concentrated under vacuum. Dissolution of the residue in a minimum amount of CH_2Cl_2 and vapor diffusion of diethyl ether into this solution yielded 65 mg (56%) of a yellow-orange powder. ^{1}H NMR (CD_2Cl_2, ppm): δ 8.87 (d, 2H), δ 8.57 (d, 1H), δ 8.42 (d, 1H), δ 8.22 (d, 2H), δ 7.75 (d, 1H), δ 7.61 (dd, 1H), δ 7.56 (dd, 2H), δ 7.19 (dd, 1H), δ 7.03 (s, 1H), δ 4.44 (s, 3H), δ 1.48 (s, 18H). Anal. Calcd. for $C_{32}H_{33}N_3O_7SF_3Re$: C, 45.38%; H, 3.93%; N, 4.96%. Found: C, 45.32%; H, 3.66%; N, 4.86%.

fac-[(4,4′-Me$_2$bpy)Re(CO)$_3$(BIQD)](OTf). A solution of *fac*-[(4,4′-Me_2bpy)Re(CO)$_3$(OTf)] (100 mg, 0.17 mmol) and benz[*g*]isoquinoline-5,10-dione (35 mg, 0.17 mmol) in CH_2Cl_2 (15 mL) was stirred for 90 min. The solution was filtered and concentrated under vacuum. Dissolution of the residue in a minimum amount of CH_2Cl_2 and vapor diffusion of diethyl ether into this solution yielded 100 mg (77%) of a pale yellow solid. The triflate anion can be exchanged for PF_6^- by dissolving the complex in a concentrated solution of NH_4PF_6 in H_2O and extracting with CH_2Cl_2. ^{1}H NMR ($CDCl_3$, ppm): δ 8.94 (s, 1H), δ 8.90 (d, 2H), δ 8.51 (d, 1H), δ 8.42 (m, 2H), δ 8.40 (d, 2H), δ 7.99 (d, 1H), δ 7.72 (m, 2H), δ 7.60 (d, 2H), δ 1.35 (s, 18H). Anal. Calcd. for $C_{29}H_{19}N_3O_8SF_3Re$: C, 42.86%; H, 2.36%; N, 5.17%. Found: C, 42.41%; H, 2.50%; N, 4.85%.

Electrochemistry. Tetrabutyl-*n*-ammonium hexafluorophosphate (TBAH), [N(*n*-$C_4H_9)_4$](PF_6), was recrystallized twice from ethanol and dried under vacuum for 10 h. Cyclic voltammograms were obtained in 0.1M TBAH/DCE solutions with a Princeton Applied Research 273 potentiostat/galvanostat interfaced to a personal computer. A silver/silver nitrate (0.1 M) reference electrode (0.314 V vs SSCE), platinum-wire auxiliary electrode, and BAS MF-2013 platinum-disk working electrode (0.31 cm^2 electrode area) were used in a standard three-compartment cell equipped for sparging with argon. Data were collected at a scan rate of 200 mV/s, and potentials are reported versus SSCE.

Spectroelectrochemistry. Absorption spectra of electrochemically reduced species were obtained in a three-compartment cell attached to a 1-cm path length quartz cuvette mounted in a Hewlett-Packard 8452D diode array spectrometer. The complex in solution (0.1M TBAH/DCE) was reduced at a platinum-mesh working electrode above the cuvette. Constant bubbling with high-purity argon provided the transport of the reduced species into the probe beam. The counter electrode was a platinum wire separated from the cathodic compartment by a glass frit, and a silver wire was used as a pseudo-reference electrode. A Princeton Applied Research 273 potentiostat/galvanostat interfaced to a personal computer was used to control the electrolysis. The charge passed through the working electrode was constantly monitored during the experiment.

Photophysical Measurements. All photophysical measurements were conducted on filtered solutions in 1-cm path length quartz cells. Solutions were degassed by sparging with solvent-saturated, high-purity argon for a minimum of 20 min. Steady-state emission and excitation spectra were collected on a SPEX Fluorolog 212 photon-counting fluorimeter interfaced to a SPEX DM1B computer. The spectra were corrected for instrument response by the procedure supplied by the manufacturer. Emission quantum yields were measured in optically dilute solutions (OD $\approx$ 0.1 at the excitation wavelength) by using a previously described procedure,[38] and are reported relative to *fac*-[(bpy)Re(CO)$_3$(4-Etpy)](PF_6) (ϕ_{em} = 0.13 in DCE at 296 K)[38] or [Os(bpy)$_3$](PF_6)$_2$ (ϕ_{em} = 0.005 in CH_3CN at 296 K).[16]

Nanosecond emission lifetimes were measured following laser flash excitation with a PRA LN1000 nitrogen laser and a PRA LN102 dye laser as described previously.[38] Emission was monitored at 90° relative to the excitation with a McPherson 272 grating monochromator and a Hammamatsu R928 photomultiplier operating within the range −600 to −750 V. The output was recorded on a LeCroy 7200A digital oscilloscope, and the digitized traces were fit to either single- or double-exponential decays by using a Levenberg−Marquardt routine. Samples had an absorbance of ~0.1 at the excitation wavelength.

Nanosecond transient absorption spectra and kinetic traces were obtained for samples with an absorbance of 0.3−0.5 at the excitation wavelength. The third harmonic of a Quanta-Ray DCR-2A Nd:YAG laser was used to pump a Quanta-Ray PDL-2 dye laser to produce excitation pulses of ~2 mJ/pulse. The excitation beam was expanded with a Gallilean telescope and then vertically compressed with a cylindrical lens to provide a rectangular cross-section at the sample cell. The probe beam was at an angle of 90° relative to excitation and was coincident with the excited volume of sample along the major axis of the excitation cross-section. The probe beam was provided by a 150 W pulsed Xe arc lamp, and the signal was measured with an Applied Photophysics f/3.4 grating monochromator and a five-stage photomultiplier. The resulting output was collected with a LeCroy 7200A digital oscilloscope interfaced to a personal computer. Electronic control and synchronization of the laser, probe, and oscilloscope were provided by electronics of our own design. Appropriate Oriel cutoff filters were used to exclude high-energy probe and scattered excitation light. Transient absorption decays were fit to single- or double-exponential decays by using a Levenberg−Marquardt routine.

Time-Resolved Infrared Measurements. Infrared measurements utilized a BioRad FTS 60A/896 step-scan interferometer as previously described.[51] Samples were excited at 355 nm by using the third harmonic of a Nd:YAG laser (Spectra Physics GCR-11, 7 ns pulse width, operated at 10 Hz). Data acquisition was gated between the laser pulse and 500 ns for TRIR spectra. Ground-state spectra were acquired as an average of 64 scans, and excited-state spectra an average of 32 scans.

Time-resolved infrared (TRIR) spectra were measured in DCE. Sample concentrations were adjusted to give an IR absorbance of approximately 1.0 for the ground-state CO bands. The sample cell and sample solutions were deoxygenated by sparging with argon for 15 min. Solutions were transferred to the cell under an inert atmosphere. Spectra were acquired in blocks of 16 scans to ensure sample integrity. No sample decomposition was observed during the acquisition periods.

Raman Measurements. Resonance Raman (RR) spectra were acquired by using continuous wave excitation from a Coherent Innova 400 Ar^+ laser. The scattered radiation was collected in a 135° backscattering geometry and passed into a SPEX 1877D triple monochromator and detected with a liquid nitrogen cooled Photometrics Model CH210 CCD.

Time-resolved resonance Raman (TR^3) spectra were measured by using the third harmonic (354.7 nm) of a Quanta-Ray DCR-2A pulsed Nd:YAG laser both to create the excited state and as a source for the Raman scattering. The scattered radiation was collected in a 135° backscattering geometry into a SPEX 1877 Triplemate spectrometer equipped with an 1800 grooves/mm grating. The Raman signal was detected by a Princeton Instruments IRY-700G optical multichannel analyzer operating in the gated mode with a ST-110 OSMA detector-controller.

TABLE 1: Crystallographic Data for *fac*-[(4,4′-^{t}Bu$_2$bpy)Re(CO)$_3$(ONQ)]

formula	$ReC_{35}H_{39}N_2O_7$
space group	$P2_1/n$
FW	785.90
a, Å	11.3422 (11)
b, Å	10.9911 (14)
c, Å	27.316 (5)
β, deg	95.605 (11)
V, Å^3	3389.1 (8)
Z	4
μ (mm^{-1})	3.67
D_{calc}, Mg m^{-3}	1.540
R_f	0.061
R_w	0.073
NO[$I > 2\sigma(I)$][a]	2815
NO	4377
quality of fit indicator	1.89
largest shift/esd	0.015

[a] NO = number of observations.

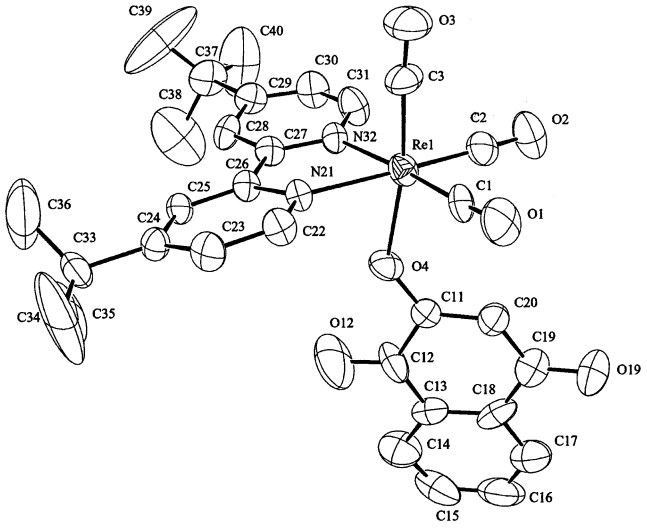

Figure 1. ORTEP diagram for *fac*-[(4,4′-^{t}Bu$_2$bpy)Re(CO)$_3$(ONQ)]. Bond lengths and angles are listed in Table 2.

Timing was controlled by a Princeton Instruments FG-100 pulse generator. The final spectra were the result of 9 min of total integration time. Laser power was between 3 and 5 mJ per pulse. Data collection and storage were controlled by an IBM AT with Princeton Instruments SMA software. All Raman spectra were acquired at ~4 mM in DCE. Samples for time-resolved resonance Raman measurements were degassed by sparging with argon.

X-ray Crystal Structure. Crystals of *fac*-[(4,4′-^{t}Bu$_2$bpy)-Re(CO)$_3$(ONQ)] suitable for X-ray diffractometry were grown by vapor diffusion of diethyl ether into a CH_2Cl_2 solution of the complex. Data were collected on a Rigaku AFC6/S diffractometer with Mo Kα radiation, a graphite monochromator, and the $\theta/2\theta$ scan mode. The software package used was NRCVAX.[50] The data collection and analysis parameters are listed in Table 1.

Analysis. Emission spectra were fit by a one-mode Franck−Condon analysis as previously described.[47]

Results

Structure of *fac*-[(4,4′-^{t}Bu$_2$bpy)Re(CO)$_3$(ONQ)]. The structure of *fac*-[(4,4′-^{t}Bu$_2$bpy)Re(CO)$_3$(ONQ)] is shown in Figure 1. It illustrates the expected facial coordination geometry of an octahedral Re(I) tricarbonyl complex with ONQ bound as a typical aryloxide ligand. The coordination geometry is distorted away from a true octahedron. The bite angle of the bound (4,4′-^{t}Bu$_2$bpy) ligand is $\angle N_{21}-Re-N_{32} = 74.4(5)°$ with the in-plane C−Re−N angles varying from 100.9(6)° (C_1-Re-N_{32}) to 96.3(6)° (C_2-Re-N_{32}). The aryloxide ligand is bent away from the in-plane CO ligands with $\angle C_3-Re-O_4 = 120.1(6)°$. There is no evidence for a structural trans effect exerted by the aryloxide ligand because the trans Re−CO, Re−C_3 bond distance of 1.885(20) Å is the same within experimental error as Re−C_1 at 1.887(18) Å. The Re−O bond length is 2.133(11) Å. Crystallographic data are listed in Table 1 and bond lengths and angles in Table 2.

TABLE 2: Important Bond Lengths (Å) and Angles (deg) in *fac*-[(4,4′-^{t}Bu$_2$bpy)Re(CO)$_3$(ONQ)] According to the Numbering Scheme in Figure 1

Re(1)−C(1)	1.887 (18)	C(3)−Re(1)−N(21)	93.8 (7)
Re(1)−C(2)	1.851 (23)	C(3)−Re(1)−N(32)	92.7 (7)
Re(1)−C(3)	1.885 (20)	O(4)−Re(1)−N(21)	78.4 (5)
Re(1)−O(4)	2.133 (11)	O(4)−Re(1)−N(32)	81.2 (5)
Re(1)−N(21)	2.150 (12)	N(21)−Re(1)−N(32)	74.4 (5)
Re(1)−N(32)	2.183 (13)	Re(1)−C(1)−O(1)	176.5 (16)
C(1)−O(1)	1.176 (23)	Re(1)−C(2)−O(2)	178.0 (16)
C(2)−O(2)	1.18 (3)	Re(1)−C(3)−O(3)	176.4 (17)
C(3)−O(3)	1.14 (3)	Re(1)−O(4)−C(11)	133.2 (10)
O(4)−C(11)	1.302 (24)	O(4)−C(11)−C(12)	114.7 (17)
C(11)−C(12)	1.45 (3)	O(4)−C(11)−C(20)	127.7 (16)
C(11)−C(20)	1.35 (3)	C(12)−C(11)−C(20)	117.6 (19)
C(12)−O(12)	1.23 (3)	C(11)−C(12)−O(12)	119.8 (22)
C(12)−C(13)	1.47 (3)	C(11)−C(12)−C(13)	123.0 (20)
C(13)−C(14)	1.35 (4)	O(12)−C(12)−C(13)	117.2 (20)
C(13)−C(18)	1.40 (4)	C(12)−C(13)−C(14)	121.3 (23)
C(14)−C(15)	1.37 (5)	C(12)−C(13)−C(18)	115.1 (20)
C(15)−C(16)	1.37 (5)	C(14)−C(13)−C(18)	123.5 (22)
C(16)−C(17)	1.37 (4)	C(13)−C(14)−C(15)	116 (3)
C(17)−C(18)	1.36 (4)	C(14)−C(15)−C(16)	123 (3)
C(18)−C(19)	1.51 (3)	C(15)−C(16)−C(17)	118 (3)
C(19)−O(19)	1.22 (3)	C(16)−C(17)−C(18)	121 (3)
C(19)−C(20)	1.39 (3)	C(13)−C(18)−C(17)	117.6 (23)
C(1)−Re(1)−C(2)	88.3 (7)	C(13)−C(18)−C(19)	121.8 (20)
C(1)−Re(1)−C(3)	88.3 (8)	C(17)−C(18)−C(19)	120.6 (23)
C(1)−Re(1)−O(4)	97.3 (6)	C(18)−C(19)−O(19)	119.1 (20)
C(1)−Re(1)−N(21)	100.9 (6)	C(18)−C(19)−C(20)	117.3 (20)
C(1)−Re(1)−N(32)	175.2 (6)	O(19)−C(19)−C(20)	123.6 (20)
C(2)−Re(1)−C(3)	90.1 (9)	C(11)−C(20)−C(19)	124.7 (19)
C(2)−Re(1)−O(4)	96.9 (7)	Re(1)−N(21)−C(22)	125.8 (11)
C(2)−Re(1)−N(21)	170.1 (6)	Re(1)−N(21)−C(26)	117.9 (10)
C(2)−Re(1)−N(32)	96.3 (6)	Re(1)−N(32)−C(27)	117.1 (11)
C(3)−Re(1)−O(4)	171.2 (7)	Re(1)−N(32)−C(31)	124.9 (12)

Spectral and Electrochemical Data. UV−vis spectra of the complexes are shown in Figure 2, and λ_{max} values for the lowest-energy absorption bands are summarized in Table 3. Dry DCE was the solvent of choice for these and other measurements due to the sensitivity of the aryloxide ligands to solvolysis in the presence of even trace amounts of water.

There is evidence in the spectrum of *fac*-[(4,4′-Me$_2$bpy)Re-(CO)$_3$(BIQD)]$^+$ for low-energy dπ(Re^I) → π^*(BIQD) bands, convoluted with dπ(Re^I) → π^*(4,4′-Me$_2$bpy) bands in the same region. Related dπ(Re^I) → π^*(LA) bands do not appear for the other complexes. These bands were investigated further for the BIQD complex by excitation-dependent resonance Raman spectroscopy. Raman scattering with excitation at 364 nm resulted in resonantly enhanced bands at 1035, 1201, 1285, 1320, 1494, and 1555 cm^{-1}, characteristic of 4,4′-Me$_2$bpy as the acceptor ligand and consistent with resonance enhancement by a Re^I → 4,4′-Me$_2$bpy transition. Bands at 1612 and 1683 cm^{-1} are also enhanced and of roughly comparable intensity. These are mixed C=C and quinone C=O stretches on the BIQD ligand.[52] The same bands were enhanced with excitation at 458 and 476 nm but with the quinone bands enhanced by a factor of 5 compared to the bipyridine bands.

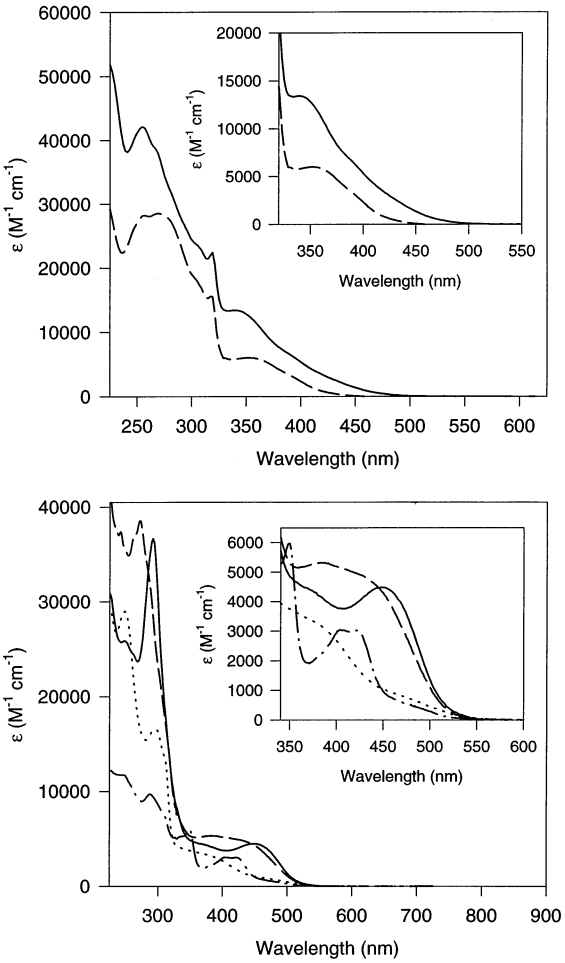

Figure 2. Top: UV−vis absorption spectra in 1,2 -dichloroethane for *fac*-[(4,4′-Me_2bpy)Re(CO)$_3$(BIQD)](CF_3SO_3) (—) and *fac*-[(4,4′-Me_2-bpy)Re(CO)$_3$(4-Etpy)](PF_6) (− − −). Bottom: UV−vis absorption spectra in 1,2 -dichloroethane for *fac*-[(4,4′-^{t}Bu$_2$bpy)Re(CO)$_3$(OPh)] (•••), *fac*-[(4,4′-^{t}Bu$_2$bpy)Re(CO)$_3$(ONQ)] (− − −), *fac*-[(4,4′-Me_2bpy)-Re(CO)$_3$]$_2$(AFA) (−•−) and *fac*-[(4,4′-^{t}Bu$_2$bpy)Re(CO)$_3$(OQD)](PF_6) (—). The inserts show enlarged views of the low energy portions of the spectra.

Ground-state infrared ν(CO) band energies and electrochemical results obtained by cyclic voltammetry in 0.1 M TBAH/DCE are summarized in Table 3.

Emission. Emission spectra in DCE are shown in Figure 3 and λ_{max} values, emission quantum yields (ϕ_{em}), and lifetimes (τ) are listed in Table 4. The slight shoulder at 550 nm in the emission spectrum of the AFA dimer was observed for several different preparations of the complex, and appears to be intrinsic.

Emission decays were fit to the exponential function, $I_t/I_0 = \exp(-kt)$ (with I_t and I_0 the emission intensity at times t and 0, respectively) and fit by using a Levenberg−Marquardt routine as previously described.[47]

There is a good match between absorption and excitation spectra for *fac*-[(4,4′-Me_2bpy)Re(CO)$_3$(BIQD)]$^+$, *fac*-[(4,4′-^{t}Bu$_2$-bpy)Re(CO)$_3$(OQD)], and *fac*-[(4,4′-Me_2bpy)Re(CO)$_3$]$_2$(AFA) above 350 nm. For *fac*-[(4,4′-^{t}Bu$_2$bpy)Re(CO)$_3$(ONQ)], the excitation spectrum failed to reveal the low-energy absorption feature at ∼400 nm in Figure 2. There was a better match with the absorption spectrum for the $^-$OPh model complex.

Emission spectra were fit by using a one-mode Franck−Condon analysis described previously.[47] The parameters that result from the analysis are the $\upsilon^* = 0 \rightarrow \upsilon = 0$ energy gap, E_0, the full bandwidth at half-height for a single vibronic component, $\Delta\bar{\nu}_{1/2}$, the quantum spacing for the average acceptor mode, $\hbar\omega$, and its electron-vibrational coupling constant, S. Results are summarized in Table 5, and the emission spectrum and fit for *fac*-[(4,4′-Me_2bpy)Re(CO)$_3$(BIQD)]$^+$ are shown in Figure 4. The quantum spacing, $\hbar\omega$, was varied for each complex in order to obtain the best fit. Some of the fits were difficult due to the low quantum yields for emission, and this is reflected in the standard deviations of the fitting parameters.

Emission from *fac*-[(4,4′-^{t}Bu$_2$bpy)Re(CO)$_3$(OPh)] is weak and poorly defined, and the fit slightly dependent on $\hbar\omega$. The slight contribution to emission from the 550 nm shoulder in *fac*-[(4,4′-Me_2bpy)Re(CO)$_3$]$_2$(AFA) was deconvoluted by discarding the data points from 16 500 to 22 000 cm^{-1}. This increased the inter-parameter correlations making the fits weakly dependent on $\hbar\omega$.

Transient Absorption. Transient absorption difference spectra were acquired in DCE following laser flash excitation at 364 nm. The difference spectra for *fac*-[(4,4′-Me_2bpy)Re(CO)$_3$-(BIQD)]$^+$ and *fac*-[(4,4′-^{t}Bu$_2$bpy)Re^I(CO)$_3$(OQD)]$^+$ are shown in Figure 5, with spectra for the ONQ and AFA complexes available as supplementary information. In all cases, the transients that formed appeared during the ∼4 ns laser pulse.

The transient absorption decays were fit to the exponential decay function

$$A_t = A_0 \exp(-kt) \tag{1}$$

with A_t and A_0 the absorbances at times t and 0, respectively, and k the decay rate constant. Rate constants are listed in Table 4. Decays for the ONQ complex were nonexponential but could be fit to the biexponential function

$$A_t = A_{0,1} \exp(-k_1 t) + A_{0,2} \exp(-k_2 t) \tag{2}$$

with $k_1 = 4.0 \times 10^7$ s^{-1} and $k_2 = 9.4 \times 10^5$ s^{-1} in DCE at 296 K.

Spectroelectrochemistry. Reduction of the BIQD complex in 0.1 M TBAH/DCE occurred with $n = 1.0$. In the spectrum of the reduced complex, absorption features appeared at ∼580 and ∼640 nm, near the features observed in the transient absorption difference spectrum of the BIQD complex in Figure 5. A shoulder also appeared at ∼390 nm. For the other chromophore−quencher complexes, reduction was chemically irreversible.

Time-Resolved Infrared (TRIR). In the ground-state infrared spectrum of the OQD complex in DCE, ν(CO) bands appear at 2019, 1909, and 1900 cm^{-1} arising from the A′(1), A′(2), and A″ modes in C_s symmetry.[53] In the TRIR spectrum, three bands also appear, shifted to slightly higher energies at 2023, 1936, and 1908 cm^{-1}.

Discussion

Before analyzing the electron-transfer data, it is necessary to analyze the spectroscopic and photophysical properties of the chromophore−quencher complexes. They are revealing as to the electronic and molecular structures of the transients reached following laser flash photolysis.

Electronic Structure of the Photochemical Transients. The electrochemical data in Table 3 establish that the quinone ligands are better acceptors than the 4,4′-R_2bpy ligands. There is evidence for direct dπ(Re) → π*(LA) absorptions for the BIQD complex in the low-energy part of the spectrum in Figure 2, as shown by the resonance Raman results.

Emission from *fac*-[(4,4′-Me_2bpy)Re(CO)$_3$(BIQD)]$^+$ is significantly red-shifted and decreased in intensity compared to the 4-Etpy model complex. This can be explained by Re^I →

TABLE 3: Spectral and Electrochemical Data in 1,2-Dichloroethane at 296 K

complex	λ_{max}, nm[c] (ϵ, M^{-1} cm^{-1})	ν(CO), cm^{-1}	$E_{1/2}(Re^{II/I})$, V	$E_{1/2}(LA^{0/-})$, V	$E_{1/2}(4,4'\text{-}R_2bpy^{0/-})$, V
$[(4,4'\text{-}Me_2bpy)Re(CO)_3(4\text{-}Etpy)]^{+}$ [a]	351 (6.0×10^4)	2034; 1928	1.78[d]		−1.16[d]
$[(4,4'\text{-}Me_2bpy)Re(CO)_3(BIQD)]^{+}$ [b]	339 (1.3×10^5)	2035; 1921	*e*	−0.39	−1.31
$[(4,4'\text{-}^tBu_2bpy)Re(CO)_3(OPh)]$	384 (3.2×10^4)	2011; 1900; 1878	0.88[f]		−1.46
	470 (9.0×10^3)				
$[(4,4'\text{-}^tBu_2bpy)Re(CO)_3(ONQ)]$	387 (5.3×10^4)	2017; 1909; 1896	1.29[f]	−1.13[f]	−1.48
	435 (4.9×10^4)				
$[(4,4'\text{-}Me_2bpy)(CO)_3Re]_2(AFA)$	404 (3.0×10^4)	2017; 1884	*g*	*g*	*g*
	421 (3.0×10^4)				
	480 (7.0×10^3)				
$[(4,4'\text{-}^tBu_2bpy)Re(CO)_3(OQD)]^{+}$ [b]	449 (4.5×10^4)	2019; 1909; 1900	1.36[f]	−1.13	−1.47

[a] PF_6^- salt. [b] $CF_3SO_3^-$ salt. [c] Maximum for the lowest-energy, intense absorptions. Numbers in parentheses are molar absorptivities. [d] From reference.[38] Irreversible wave, $E_{p,a}$ is reported. [e] Beyond the electrochemical window. [f] Irreversible wave, $E_{p,a}$ is reported. [g] Not sufficiently soluble for electrochemical measurement.

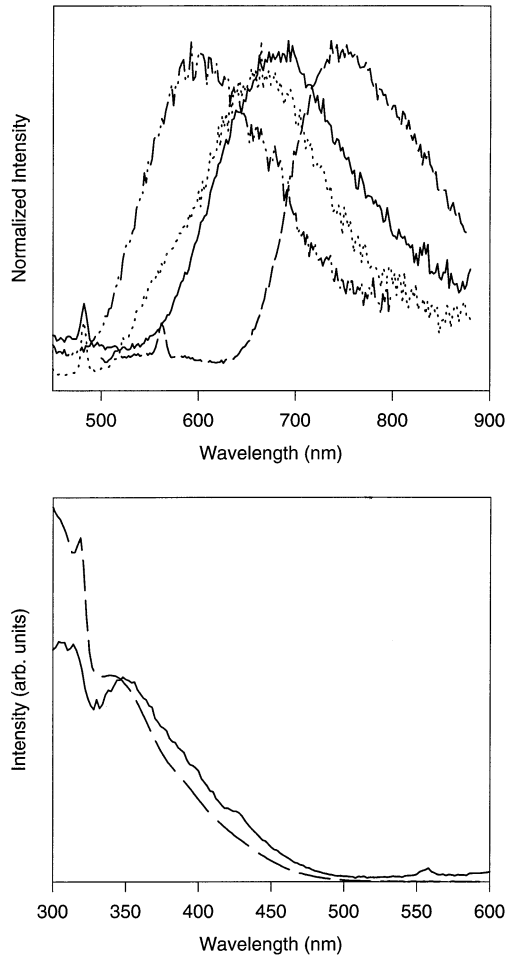

Figure 3. Top: Corrected emission spectra at room temperature in 1,2-dichloroethane for *fac*-$[(4,4'\text{-}Me_2bpy)Re(CO)_3(BIQD)](CF_3SO_3)$ (—) (420 nm excit.), *fac*-$[(4,4'\text{-}^tBu_2bpy)Re(CO)_3(ONQ)]$ (— · · · —) (377 nm excit.), *fac*-$[(4,4'\text{-}Me_2bpy)Re(CO)_3]_2(AFA)$ (···) (420 nm excit.), and *fac*-$[(4,4'\text{-}^tBu_2bpy)Re(CO)_3(OQD)](CF_3SO_3)$ (— — —) (480 nm excit.). The spectra have been normalized to a constant intensity maximum for ease of comparison. Bottom: Excitation (—) and absorption (— — —) spectra for *fac*-$[(4,4'\text{-}Me_2bpy)Re(CO)_3(BIQD)](CF_3SO_3)$ in 1,2-dichloroethane at room temperature monitored at 670 nm. The spectra are arbitrarily scaled for ease of comparison.

4,4′-Me_2bpy excitation followed by intramolecular electron transfer and emission from a $Re^{II}(BIQD^{\bullet-})$-based state. This conclusion is consistent with the transient absorption difference spectrum in Figure 5 and the enhanced intensity of the BIQD quinone bands in the ground-state resonance Raman spectrum with low-energy excitation. The ∼25 ns decay time for the transient is close to the observed 32 ns emission lifetime (Table 4), corroborating it as the origin of the short-lived emission. The good match between excitation and absorption spectra shows that efficient population of the emissive state occurs both upon $d\pi(Re) \rightarrow \pi^*(4,4'\text{-}Me_2bpy)$ excitation followed by intramolecular electron transfer, and by direct $d\pi(Re) \rightarrow \pi^*(LA)$ absorption in the low-energy visible.

A kinetic scheme is illustrated in Scheme 1 which includes the electronic configurations of the states involved. MLCT absorption in these complexes is dominated by transitions which give states of electronic configuration $^1(d\pi^5\pi^*_{bpy}{}^1)$. They are largely singlet in character. For the model complex, emission occurs from the corresponding triplets $^3(d\pi^5\pi^*_{bpy}{}^1)$. These "triplet" and "singlet" states are of mixed spin character because of spin−orbit coupling at d^5 Re^{II} ($\zeta \approx 2000$ cm^{-1}). The emitting "triplet" is actually a manifold of three closely lying states in rapid Boltzmann equilibrium which behave dynamically as a single state at or near room temperature.[54]

The emitting state for the BIQD complex is probably largely triplet in character as well. Conversion from $^1(d\pi^5\pi^*_{bpy}{}^1)$ to $^3(d\pi^5\pi^*_{bpy}{}^1)$ is known to be rapid in related Ru and Os polypyridyl complexes and the triplet(s) appear to be the states that undergo electron-transfer quenching. For the ONQ^- complex, the quenching step was observed by direct measurement and occurs with $k \approx 4 \times 10^7$ s^{-1}.

Spin is conserved in the quenching step because the operator that mixes the initial and final states and induces electron transfer does not include spin. The spin state wave function before quenching is given approximately by, $\Psi_s = {}^3\Psi_s + \alpha^1\Psi_s$, with ${}^3\Psi_s$ the pure triplet spin wave function and ${}^1\Psi_s$ the singlet spin wave function for the lowest energy singlet excited state. The mixing coefficient α depends on the spin−orbit coupling constant and the triplet−singlet energy gap. The percentage of singlet character in the initial MLCT state is 10−20%.[54] The percent of singlet character in the electron-transfer product depends on α^2 and should be less than 5%.

On the basis of an analysis presented in the following section, the magnitude of the electron-transfer matrix element arising from the $Re^{II}(BIQD^{\bullet-})$ electronic interaction in the transient is only 153 cm^{-1}, far less than the reorganizational energy associated with $BIQD^{\bullet-} \rightarrow Re^{II}$ electron transfer. Because of this, the transient is best described as a "redox-separated" (RS) state in which the electron transfer donor and acceptor sites are only moderately coupled electronically and back electron transfer occurs in the inverted region.

Emission from the model complex *fac*-$[(4,4'\text{-}^tBu_2bpy)Re(CO)_3(OPh)]$ is also red-shifted, of lower intensity, and occurs with a shorter lifetime than *fac*-$[(bpy)Re(CO)_3(4\text{-}Etpy)]^{+}$*. These are the expected consequences of replacing 4-Etpy with the σ- and π-donating ^-OPh ligand. Emission from the AFA^{2-} and OQD complexes is red-shifted even further, but the lifetimes

TABLE 4: Spectroscopic and Photophysical Properties in DCE at 296 K

complex	λ^{em}_{max}, nm	ϕ_{em}[d]	τ_{em}, ns[f]	τ_{abs}, ns (k, s^{-1})[g]
[(4,4′-Me_2bpy)Re(CO)$_3$(4-Etpy)]$^+$ [a]	568	0.129	510 ± 20	
[(4,4′-Me_2bpy)Re(CO)$_3$(BIQD)]$^+$ [b]	688	0.0018	32 ± 1	25 ± 1 (4.0×10^7)
[(4,4′-^{t}Bu$_2$bpy)Re(CO)$_3$(OPh)]	628[c]	0.0006	84 ± 10	
[(4,4′-^{t}Bu$_2$bpy)Re(CO)$_3$(ONQ)]	602	0.0005	79 ± 7	25 (4×10^7),[h] 1.0×10^3 (1×10^6)
[(4,4′-Me_2bpy)(CO)$_3$Re]$_2$(AFA)	664	0.001	$4.1 \pm 1.5 \times 10^3$	$5.6 \pm 0.3 \times 10^3$ (1.8×10^5)
[(4,4′-^{t}Bu$_2$bpy)Re(CO)$_3$(OQD)]$^+$ [b]	748	0.0005[e]	$(16 \pm 2) \times 10^3$	$(15.2 \pm 0.7) \times 10^3$ (6.6×10^4)

[a] PF_6^- salt. [b] $CF_3SO_3^-$ salt. [c] Shoulder. [d] Emission quantum yields relative to *fac*-[(bpy)Re(CO)$_3$(4-Etpy)](PF_6) in DCE at 296 K.[38] [e] Relative to [Os(bpy)$_3$](PF_6)$_2$ in CH_3CN at 296 K. [f] Lifetimes as determined from emission decays measured at a minimum of three monitoring wavelengths. Comparable values were obtained with excitation at 376, 420, and 460 nm for BIQD. For OQD, the average value obtained with excitation at 420, 460, and 480 nm excitation is reported. [g] Lifetimes and rate constants for transient absorption decays following laser flash excitation at 364 nm. See text. [h] Decay of the Re^{II}(4,4′-^{t}Bu$_2$bpy$^{\bullet-}$) MLCT excited state.

TABLE 5: Emission Spectral Fitting Parameters in DCE at 296 K

complex	E_0, cm^{-1} [c]	S	$\Delta\bar{\nu}_{1/2}$, cm^{-1}	$\hbar\omega$, cm^{-1} [d]
[(4,4′-Me_2bpy)Re(CO)$_3$(4-Etpy)]$^+$ [a]	18900 (20)	2.14 (0.02)	2050 (27)	1186
[(4,4′-Me_2bpy)Re(CO)$_3$(BIQD)]$^+$ [b]	14900 (40)	0.81 (0.05)	2900 (67)	1625
[(4,4′-^{t}Bu$_2$bpy)Re(CO)$_3$(OPh)]	16700 (150)	1.45 (0.18)	2850 (214)	1300[e]
[(4,4′-^{t}Bu$_2$bpy)Re(CO)$_3$(ONQ)]	17200 (100)	1.25 (0.10)	3130 (155)	1606
[(4,4′-Me_2bpy)(CO)$_3$Re]$_2$(AFA)	15500 (100)	0.95 (0.12)	2830 (192)	1500[e]
[(4,4′-^{t}Bu$_2$bpy)Re(CO)$_3$(OQD)]$^+$ [b]	13600 (10)	1.11 (0.01)	1770 (17)	1376

[a] PF_6^- salt. [b] $CF_3SO_3^-$ salt. [c] Numbers in parentheses are standard deviations. [d] Values cited give the smallest standard deviation for the fit. [e] Parameter fixed arbitrarily; the overall fit was weakly dependent on the value chosen.

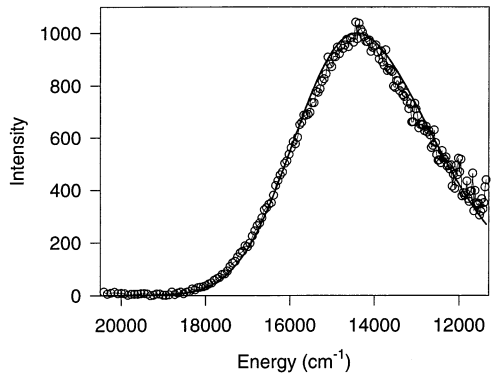

Figure 4. Normalized emission spectrum of *fac*-[(4,4′-Me_2bpy)Re(CO)$_3$(BIQD)]$^+$ in 1,2-dichloroethane at room temperature (○) and one-mode fit (—) with the parameters $E_0 = 14\,920$ cm^{-1}, $S = 0.81$, $\Delta\bar{\nu}_{1/2} = 2900$ cm^{-1} and $\hbar\omega = 1625$ cm^{-1}.

are remarkably long, Table 4. Excitation and absorption spectra match, showing that the transients are produced efficiently over a wide wavelength range by dπ(Re) → π^*(4,4′−R_2bpy) excitation.

For the AFA^{2-} complex, there is evidence for a high-energy component in the emission spectrum in the appearance of a shoulder at 550 nm (Figure 3). Emission decay at this wavelength was convoluted with the instrument response function ($\tau < 20$ ns). An excitation spectrum acquired at 550 nm coincided with the absorption maximum at 370 nm.

For the OQD complex, a bleach appears at 470 nm in the transient absorption difference spectrum consistent with oxidation at Re(I) and loss of the dπ(Re) → π^*(4,4′-^{t}Bu$_2$bpy) absorption. There are also narrow and broad features at 360 and 600 nm, respectively, consistent with formation of the reduced pyridinium form of the complex.[55−57] For the AFA^{2-} complex, there is a bleach at 410 nm, and new absorptions at 370−380 and 500 nm arising from the reduced AFA^{3-} radical anion. The radical anion of anthraquinone generated by pulse radiolysis has broad absorptions at 400 and 540 nm in CH_3CN,[58] and coordinated 4,4′-R_2bpy anion at ∼370 nm.[59]

For the ONQ^- complex, there is evidence for both short- and long-lived transients. Emission is dominated by the short-lived transient and the excitation spectrum largely matches the absorption spectrum of the $^-$OPh model, rather than the chromophore−quencher complex. Transient absorption decay data were fit to eq 2 with $\tau_1 = 25$ ns ($k = 4.0 \times 10^7$ s^{-1}) and $\tau_2 = 1$ μs ($k = 1 \times 10^6$ s^{-1}), Table 4. In the transient absorption difference spectra for the long-lived transient obtained at 90 and 300 ns after the laser pulse, a bleach appears at ∼500 nm and absorptions at 380 nm 600 nm. The more intense, short-lived emission appears to mask any red-shifted, long-lived emission from this complex. It may contribute to the difference between emission and absorption lifetimes in Table 4.

The transient reached following MLCT excitation of the OQD complex was also investigated by transient infrared measurements. Bands appear at 2019, 1909, and 1900 cm^{-1} in the ground-state spectrum arising from the A′(1), A″, and A′(2) modes in C_s symmetry. In the transient, the band at 2019 cm^{-1} is shifted to 2023 cm^{-1}, the band at 1909 cm^{-1} is shifted to 1936 cm^{-1} and the band at 1916 cm^{-1} is shifted to 1908 cm^{-1}. These shifts of 4, 37, and 8 cm^{-1} are in contrast to the Re^{II}(bpy$^{\bullet-}$) MLCT excited state of *fac*-[(bpy)Re^{I}(CO)$_3$(4-Etpy)]$^+$ for which the corresponding excited-to-ground-state shifts are 35, 84, and 27 cm^{-1}.[60,61]

Large, positive ν(CO) shifts are expected for MLCT excited states because partial oxidation decreases dπ(Re)−π^*(CO) back-bonding, which increases CO bond order. Small positive shifts are a characteristic feature of $\sigma\pi^*$ excited states.[62−64] In these excited states the "hole" resides in a metal−ligand σ bond, in this case the Re−O bond, to give the configuration σ(Re−O)$^1\pi^*$(LA)^1, rather than the dπ(Re)$^5\pi^*$(LA)^1 MLCT configuration of the BIQD assembly.

This explains the smaller ν(CO) shifts. Even though there is charge-transfer character in the transient, the site of oxidation is σ(Re−O). To zero order, this orbital is orthogonal to the dπ orbitals and to the dπ(Re)−π^*(CO) back-bonding interaction. This interpretation also explains the chemical irreversibility of the AFA^{2-}, ONQ^-, and OQD-based $Re^{II/I}$ couples. They occur

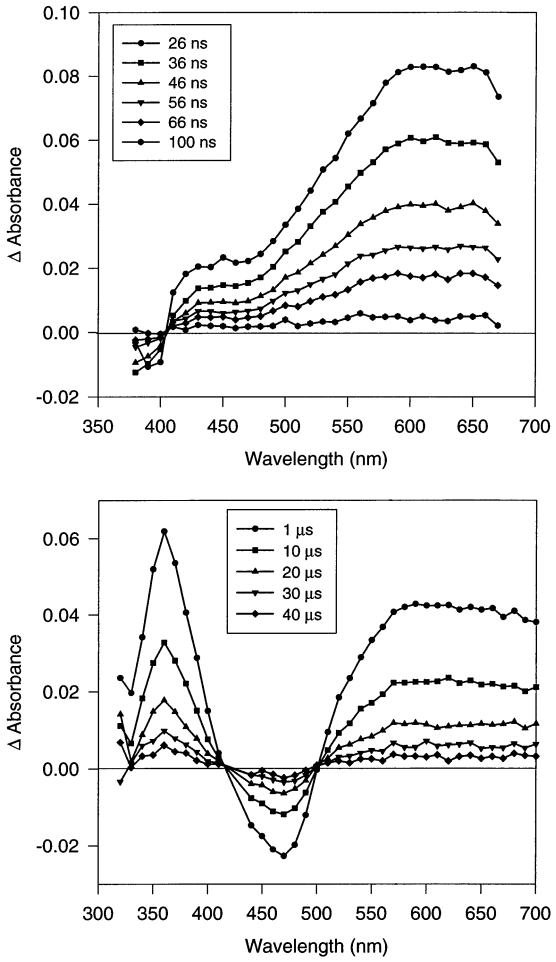

Figure 5. Top: Time-resolved absorption difference spectra for *fac*-[(4,4′-Me_2bpy)Re(CO)$_3$(BIQD)]$^+$ in 1,2-dichloroethane at room temperature following 355 nm, 4 ns pulsed, 2 mJ/pulse excitation. Bottom: Time-resolved absorption difference spectra for *fac*-[(4,4′-^{t}Bu$_2$bpy)Re(CO)$_3$(OQD)]$^+$ in 1,2-dichloroethane at room temperature following 420 nm, 4 ns pulsed, 2 mJ/pulse excitation.

SCHEME 1

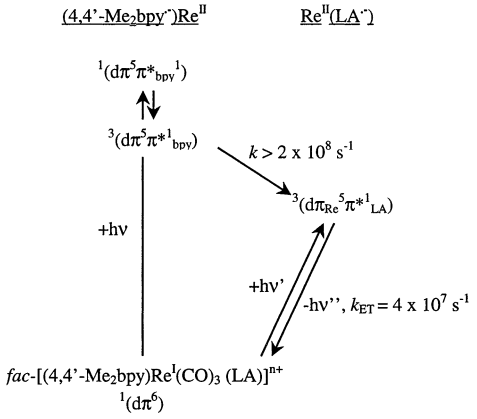

at relatively low potentials but, since oxidation occurs at the Re−O bond, oxidation leads to decomposition. The orthogonality of the dσ(Re−O) donor and π*(LA) acceptor orbitals also contributes to the very weak electronic coupling between Re^{II} and the reduced AFA and OQD ligands (next section). Weak electronic coupling is a major contributor to slow back electron transfer and the extended lifetimes of the transients.

The transients reached in this case are also best described as RS states, but with the hole at σ(Re−O) rather than dπ(Re).

SCHEME 2

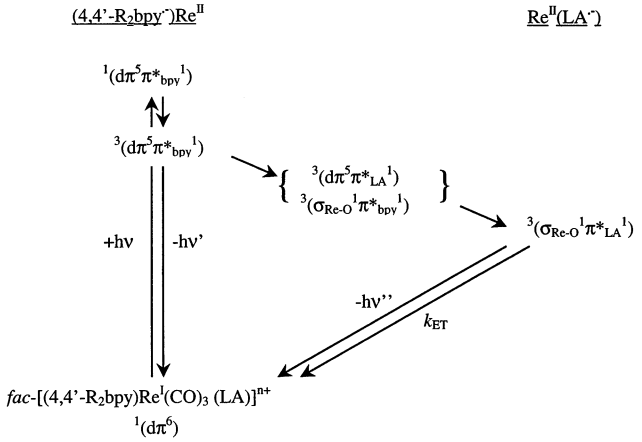

The suggested sequence of events that occurs following Re^I → π*(4,4′-R_2bpy) MLCT excitation in these cases is illustrated in Scheme 2.

In this case, initial dπ(Re^I) → π*(4,4′-R_2bpy) excitation is followed by rapid (<5 ns) formation of the Re^{II}(4,4′-R_2bpy$^{\bullet-}$) "triplet" state. For the AFA^{2-} and ONQ$^-$ complexes, there is evidence for the intermediacy of this state by the appearance of short-lived emissions at high energies. The initial MLCT state undergoes rapid interconversion to the final $\sigma-\pi$* states with $k \approx 4.0 \times 10^7$ for the ONQ$^-$ complex and $k > 2 \times 10^8$ s^{-1} for the AFA^{2-} complex. This may occur by initial π*(bpy) → π*(LA) electron transfer to give ^{3}(d$\pi^5\pi^*{}_{LA}{}^1$) followed by σ_{Re-O} → dπ(Re) electron transfer, or by electron transfer in the reverse order.

Analysis Based on Spectral Fitting Parameters. Application of a Franck−Condon analysis to emission spectral profiles with the average mode approximation gave the fitting parameters in Table 5. The bandwidth at half-height for each vibronic component, $\Delta\bar{\nu}_{1/2}$, is related to $\lambda_{o,L}$, the sum of the solvent reorganizational energy, λ_o, and the reorganzational energy contributed by low-frequency modes treated classically $\lambda_{i,L}$, by eq 3[16,65]

$$(\Delta\bar{\nu}_{1/2})^2 = 16k_B T\lambda_{o,L} \ln 2 \quad (3)$$

$\lambda_{i,L}$ is given by

$$\lambda_{i,L} = \Sigma\lambda_{i,l} = \Sigma S_l \hbar\omega_l \quad (4)$$

where the sum is over the coupled vibrations, l (those with $S_l \neq 0$).

These are inherently multi-mode processes. Based on resonance Raman measurements, there are 11 totally symmetrical ν(bpy) modes coupled to nonradiative decay of the MLCT state(s) of [Ru(bpy)$_3$]$^{2+}$*, for example.[66,67] In the average mode approximation, S is the sum of S_j values for the coupled high- and medium-frequency vibrations

$$S = \Sigma S_j \quad (5)$$

and $\hbar\omega$ is the weighted average of the quantum spacings

$$\hbar\omega = \Sigma S_j \hbar\omega_j / \Sigma S_j \quad (6)$$

It is also possible to calculate the electron-transfer matrix element arising from dπ(Re^{II}) (or σ(Re−O)) electronic coupling with π*(LA), H_{DA}, from the rate constant for radiative decay, k_r, and the emission spectral fitting parameters. k_r is related to

TABLE 6: Exited State Parameters in DCE at 296 K

complex	k_r, s^{-1} [b]	$\langle\nu^{-3}\rangle^{-1}$, cm^3 [c]	d (Å)	$\lambda_{o,L}$, cm^{-1} [d]	E_{abs}, cm^{-1} [e]	ΔG^o_{ES}, cm^{-1} [f]
$[(4,4'\text{-}Me_2bpy)Re(CO)_3(BIQD)]^{+}$ [a]	5.6×10^4	2.48×10^{12}	6	3660	23600	18600
$[(4,4'\text{-}Me_2bpy)(CO)_3Re]_2(AFA)$	2.4×10^2	2.86×10^{12}	6	3500	23900	19000
$[(4,4'\text{-}{}^tBu_2bpy)Re(CO)_3(OQD)]^{+}$ [a]	3.2×10^1	1.80×10^{12}	5	1360	17900	15000

[a] $CF_3SO_3^-$ salt. [b] Calculated from $k_r = \phi_{em}/\tau_{em}$. [c] Calculated from the emission spectra by using eq 10. [d] Calculated from eq 3 and parameters in Table 5. [e] Calculated from eq 11 and the parameters in Table 5. [f] Calculated with eq 13 and the parameters in Table 5.

the emission quantum yield and lifetime by eq 7. Values are listed in Table 6. There is no entry for the ONQ complex because the low-energy emission from the $\sigma-\sigma^*$ RS state is masked by residual MLCT emission.

$$k_r = \phi_{em}/\tau \tag{7}$$

There are two approaches to calculating H_{DA} from k_r, both based on perturbation theory and application of the Strickler−Berg equation.[68]

The transition moment is given by $M = \langle\Psi_e|\Sigma\, \mathbf{r}_n|\Psi_g\rangle$, with Ψ_e and Ψ_g the excited- and ground-state vibronic wave functions including spin, and $\mathbf{r}_n$ the electronic coordinates. The summation is over n. By assuming significant mixing only between the excited (Ψ_e) and ground-state (Ψ_g) electronic wave functions and the involvement of only two states, H_{DA} is related to k_r as shown in eq 8

$$k_r = \frac{34\pi^2 n^3}{3\hbar}(H_{DA}\Delta\mu)^2\langle\bar{\nu}\rangle \tag{8}$$

$\Delta\mu$ is the vector difference in permanent dipole moments between the ground and excited states, $\langle\bar{\nu}\rangle$ is the average emission energy which is usually taken as the emission maximum, and n is the solvent index of refraction.[21,22,24,69] Application of eq 8 requires knowledge of the excited- and ground-state dipole moments.

It is also possible to calculate H_{DA} by using the emission band shape parameters to calculate the corresponding absorption band. H_{DA} can then be calculated by applying an analysis given by Hush for intervalence transfer in electronically weakly coupled mixed-valence complexes.[65,70] This involves relating the transition moment to the oscillator strength of the absorption band.

Assuming a Gaussian band shape, k_r is related to the molar extinction coefficient ϵ_{max} in M^{-1} cm^{-1}, the absorption band energy, E_{abs} in cm^{-1}, and the spectral bandwidth $\Delta\bar{\nu}_{1/2,s}$ ($=\Delta\bar{\nu}_{1/2,s}$ for emission) in cm^{-1} as in eq 9

$$k_r = (3.05 \times 10^{-9})\, n^2\langle\bar{\nu}^{-3}\rangle^{-1}\frac{\epsilon_{max}\Delta\bar{\nu}_{1/2,s}}{E_{abs}} \tag{9}$$

$\langle\nu^{-3}\rangle^{-1}$ is defined as

$$\langle\bar{\nu}^{-3}\rangle = \frac{\int I(\nu)\,d\nu}{\int \nu^{-3} I(\nu)\,d\nu} \tag{10}$$

$I(\bar{\nu})$ is the emitted intensity at frequency $\bar{\nu}$.

E_{abs} is related to the corresponding emission maximum, E_{em}, and the spectral fitting parameters $\Delta\bar{\nu}_{1/2}$, S, and $\hbar\omega$ as in eq 11

$$E_{abs} \approx E_{em} + 2\lambda_{o,L} + 2S\hbar\omega = E_{em} + \frac{2(\Delta\bar{\nu}_{1/2,s})}{16k_B T \ln 2} + 2S\hbar\omega \tag{11}$$

The final relationship between k_r and H_{DA} is given in eq 12, with d the electron-transfer distance

$$H_{DA} = \left(\frac{E_{abs}}{nd}\right)[(1.39 \times 10^5)k_r\langle\bar{\nu}^{-3}\rangle]^{1/2} \tag{12}$$

The free energy content of the emitting state above the ground state, ΔG^o_{ES}, is given by

$$\Delta G^o_{ES} = E_0 + \lambda_{o,L} = E_0 + \frac{(\Delta\bar{\nu}_{1/2,s})^2}{16k_B T \ln 2} \tag{13}$$

For back electron transfer, $\Delta G^o = -\Delta G^o_{ES}$. The relationships in eqs 3−13 and the data in Tables 4−6 allow $\lambda_{o,L}$ to be calculated from eq 3, E_{abs} from eq 11, H_{DA} from eq 12, ϵ_{max} from eq 9, and ΔG^o_{ES} from eq 13. The results are tabulated in Tables 6 and 7.

Molecular and Electronic Structure. The results of the analysis in the previous section give further insight into the electronic and molecular structures of the transients.

For the aryloxy complexes, the electronic coupling matrix element is small, 9.4 cm^{-1} for the AFA^{2-} complex and 3.9 cm^{-1} for the OQD complex. This is consistent with the orthogonal orbital relationship between the donor and acceptor orbitals in the $\sigma\pi^*$ RS states and their anticipated triplet character.[71] On the basis of this analysis, formation of these states by direct excitation is unimportant. The corresponding absorptions are predicted to occur at 418 nm with $\epsilon = 0.078$ M^{-1} cm^{-1} for the AFA^{2-} complex, and at $E_{abs} \approx 560$ nm with $\epsilon = 0.016$ M^{-1} cm^{-1} for the OQD complex.

Electronic coupling is modest even for the BIQD complex (153 cm^{-1}). The calculated absorption for direct excitation is predicted to occur at 424 nm with $\epsilon = 22$ M^{-1} cm^{-1}, which would appear in the tail of the absorption spectrum shown in Figure 2. Enhancement of the quinone-based BIQD modes in excitation-dependent resonance Raman spectra and evidence for $Re^I \rightarrow$ BIQD absorption can be attributed to transitions to the corresponding singlet states which are close in energy.

The transient RS states return nonradiatively to the ground state by $LA^- \rightarrow Re^{II}$ electron transfer. These reactions occur in the inverted region, since, based on the parameters in Table 6, $-\Delta G^o = \Delta G^o_{ES} > \lambda$ ($=\lambda_{o,L} + S\hbar\omega$).

Although the electronic configurations of the transients are those of $\sigma\pi^*$ or MLCT excited states, they are *not* excited states. The relationship between the two is analogous to that between localized and delocalized forms of mixed-valence complexes.[70,77] For example, in the series $[(NH_3)_5Ru(4,4'\text{-bpyridine})Ru(NH_3)_5]^{3+}$ (**1**),[72−74] $[(NH_3)_5Ru(pz)Ru(NH_3)_5]^{5+}$ (**2**, pz is pyrazine),[75] and $[(NH_3)_5Os(pz)Os(NH_3)_5]^{5+}$(**3**),[76] there is a transition from electronically localized to delocalized behavior. Electronic coupling in **1** is relatively weak, which localizes the exchanging electron. This maximizes structural differences and solvent polarization. Electronic coupling is promoted by $d\pi-\pi,\pi^*-d\pi$ mixing across the ligand bridge. Increased electronic coupling in **2** partly delocalizes the exchanging electron, decreasing structural differences and averaging the solvent.[77] In **3**, the odd electron is delocalized in a $d\pi-d\pi$ molecular orbital with considerable pyrazine mixing.

TABLE 7: Comparison of Calculated and Experimental Back Electron Transfer Rate Constants in DCE at 296 K

complex	ϵ_{max}, M^{-1} cm^{-1} [b]	H_{DA}, cm^{-1} [c]	ln[F(calc)][d]	k_{obs}, s^{-1} [e]	$k_{b,calc}$, s^{-1} [f]
[(4,4′-Me_2bpy)Re(CO)$_3$(BIQD)]$^+$ [a]	22	153	−12.2	4.0×10^7	1.1×10^7
[(4,4′-Me_2bpy)(CO)$_3$Re]$_2$(AFA)	0.078	9.4	−13.5	1.78×10^5	1.2×10^4
[(4,4′-^{t}Bu$_2$bpy)Re(CO)$_3$(OQD)]$^+$ [a]	0.016	3.9	−12.1	6.58×10^4	9.2×10^3

[a] $CF_3SO_3^-$ salt. [b] Calculated from eq 9 and the parameters in Tables 5 and 6. [c] Calculated from eq 12 and the parameters in this table and Tables 4 and 5. [d] Calculated with eq 16a and the parameters in Table 5. [e] From Table 4. [f] Calculated from eq 14 or 16.

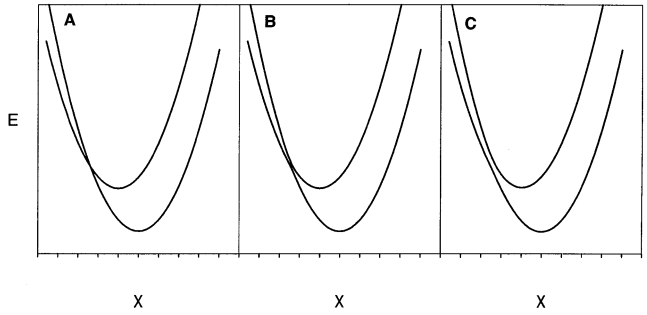

Figure 6. Schematic energy-coordinate diagrams illustrating the effect of increasing electronic coupling and the transition between electron transfer in the inverted region (A) to nonradiative decay (C). The energy curves were calculated by using the following equations: $E_1 = [\lambda(2X^2 - 2X + 1 + \Delta E_0]/2 - \{[\lambda(2X - 1) - \Delta E_0]^2 + 4H_{DA}^2\}^{1/2}/2$; $E_2 = [\lambda(2X^2 - 2X + 1 + \Delta E_0]/2 + \{[\lambda(2X - 1) - \Delta E_0]^2 + 4H_{DA}^2\}^{1/2}/2$ and the parameters $\lambda = 5000$ cm^{-1}, $\Delta E_0 = 19\,000$ cm^{-1} and (A) $H_{DA} = 0$ cm^{-1}, (B) $H_{DA} = 1000$ cm^{-1}, and (C) $H_{DA} = 2500$ cm^{-1}.

Figure 6 illustrates the influence of increasing electronic coupling on the energy-coordinate curves for electron transfer in the inverted region. The curves illustrate the variation in energy along the normal mode of a coupled vibration as H_{DA} increases.[78,79] For the case in Figure 6A, $H_{DA} \approx 0$, which is the case for the AFA^{2-} and OQD complexes. Electron transfer in these complexes occurs between electronically weakly coupled sites with a large free energy change, ΔG^o. As noted above, they are "redox-separated states" and conversion to the ground state occurs by a combination of radiative decay and nonradiative decay by electron transfer. Electron transfer is dominated by nuclear tunneling through vibrational overlap in the coupled medium- and high-frequency ν(4,4′-X_2bpy) and $\nu(LA^{\bullet-})$ modes rather than by classical barrier-crossing at the intersection between energy curves.[80,81]

The effect of increasing H_{DA}, as in the BIQD complex, is illustrated in Figure 6B. As in mixed-valence complexes, enhanced electronic coupling mixes the electronic character of the donor and acceptor which decreases the classical barrier to electron transfer.

The equivalent to the delocalized, mixed-valence case is shown in Figure 6C. In this limit, there is strong electronic coupling and the zero-order energy surfaces are highly mixed to give well separated excited- and ground-state surfaces. This is the case for the MLCT excited state of $[Ru(bpy)_3]^{2+}$, $[Ru^{III}(bpy^{\bullet-})(bpy)_2]^{2+*}$. In this limit, excited-state decay occurs by a combination of emission and nonradiative decay (k_{nr}). The nonradiative transition is vibronically induced by coupling with a "promoting" mode or modes. The interconversion between states involves a significant change in radial electronic distribution but not electron transfer.[12,16,81,82]

There is also information in the spectroscopic data about the structural changes that accompany electron transfer. Values of $\hbar\omega$ for the quinone-based BIQD and AFA^{2-} acceptors are significantly higher (1500−1600 cm^{-1}) than in typical polypyridyl complexes (∼1300 cm^{-1}). This is a consequence of the addition to the average mode approximation, eq 6, of the coupled quinone-based modes at 1612 and 1683 cm^{-1}. It is also consistent with the excitation-dependent resonance Raman results on the BIQD complex.

The values for $\Delta\bar{\nu}_{1/2}$ are also larger for the quinone complexes, ∼3000 cm^{-1} compared to ∼1800 cm^{-1}. This may be a consequence of specific solvent interactions with the quinone oxygen atoms in the semiquinone-based electron-transfer intermediates, which increases solvent coupling to electron transfer.

Calculation of Electron-Transfer Rate Constants. From electron transfer theory for a single coupled medium- or high-frequency mode, the rate constant for electron transfer is given by eq 14[9−13,78,83,84]

$$k_{ET} = \nu_{ET} \exp(-S) \sum_{\upsilon'} \frac{S^{\upsilon'}}{\upsilon'!} \exp\left(-\frac{(|\Delta G^o| + \upsilon'\hbar\omega + \lambda_{o,L})^2}{4\lambda_{o,L}k_BT}\right) \quad (14)$$

This equation utilizes the average-mode approximation and is valid in the limit $\hbar\omega \gg k_BT$. The summation is from the $\upsilon = 0$ vibrational level in the initial state to all υ' levels in the final state. The remaining parameters were defined previously. ν_{ET} is the frequency factor for electron transfer, which in the nonadiabatic limit is given by

$$\nu_{ET} = \frac{2\pi H_{DA}^2}{\hbar}\left(\frac{1}{2\pi\hbar\,\omega E_0}\right)^{1/2} \quad (15)$$

In the limit $E_0 \gg S\hbar\omega$, the sum in eq 14 is accurately given by the "energy gap law" result in eq 16, with F(calc) the Franck−Condon weighted density of states.[7,16,81,82,85]

$$k_{ET} = \nu_{ET} \exp(-S) \exp\left(-\frac{\gamma E_0}{\pi\omega}\right) \exp\left\{\left(\frac{\gamma + 1}{\hbar\omega}\right)^2 k_BT\lambda_{o,L}\right\} \quad (16a)$$

$$\gamma = \ln\left(\frac{E_0}{S\hbar\omega}\right) - 1 \quad (16b)$$

$$\ln k_{ET} = \ln \nu_{ET} + \ln[F(\text{calc})] \quad (16c)$$

All the parameters that appear in eqs 14−16 are available from the emission spectral fitting results and k_r. Calculated values of k_{ET} are compared with experimental values in Table 7. The same values were obtained by using either eq 14 or eq 16. The ONQ complex is not included in the comparison because the emission from the RS state is masked by the more intense MLCT emission.

Inspection of the data in Table 7 shows that there is agreement between calculated and experimental rate constants that ranges from a factor of ∼4 for the BIQD complex and to within a factor of ∼15 for the AFA^{2-} complex. These examples join a limited number of others based on organic donor−acceptor complexes, and nonradiative decay of MLCT excited states for which it has been possible to calculate rate constants with reasonable accuracy by using spectroscopically derived parameters.[1,14,16,21−23,69]

Given the approximations involved, the agreement between calculated and experimental values is reasonable. However, it is notable that the calculated values are lower than the experimental values in all three cases. There may be contributions to these discrepancies from the low emission intensities with a concomitant uncertainty in the emission spectral fitting parameters, and the use of the calculated absorption band to evaluate H_{DA}.

There may be another explanation. The RS states are largely triplet in character and only weakly coupled to the singlet ground states by spin−orbit coupling. There are additional, largely singlet RS states, ^{1}RS, at higher energy. In the MLCT excited state manifolds of Ru and Os polypyridyl complexes, the lowest lying, largely singlet states are 1000's of cm^{-1} to higher energy. In the RS states of these Re complexes, where spin−spin coupling is expected to be weak to moderate, the energy gaps to ^{1}RS may be small and ^{1}RS thermally accessible.

This opens an additional, thermally activated channel for back electron transfer, ^{3}MLCT → ^{3}RS ⇆ ^{1}RS → ^{1}GS. There is negligible spin inhibition to back electron transfer and the transition ^{1}RS → ^{1}GS. Interconversion between ^{3}RS and ^{1}RS states is expected to be rapid because of spin−orbit induced paramagnetic relaxation in the dπ^5 Re^{II} core.[86] It should be possible to explore the intervention of a ^{1}RS channel by temperature-dependent and/or magnetic field-dependent lifetime measurements.[71,86]

The successful use of eq 15 for ν_{ET} in eq 16, even for the BIQD complex for which $H_{DA} \approx 153$ cm^{-1}, is notable. These equations are derived from time-dependent perturbation theory. Application of eq 15 assumes the "nonadiabatic" limit with ν_{ET} dictated by the electron tunneling frequency. In thermally activated processes in the normal region, H_{DA} values of this magnitude would be sufficient to ensure "adiabatic" electron transfer with the transferring electron always in equilibrium with the coupled nuclear motion or motions. Under these conditions, the frequency of barrier crossing is dictated by the dynamics of the slowest coupled nuclear motion or motions, typically in the solvent, rather than by H_{DA}.

Equation 15 has even been applied successfully to electron transfer in organic donor−acceptor complexes by Gould, Farid, and co-workers, where H_{DA} is 1000's of cm^{-1}.[20−24,69] The success of this approach may be a consequence of the fact that these reactions occur deeply in the inverted region and are dominated by vibrational quantum transitions. There is no requirement in the dynamics for thermal activation to a barrier crossing dominated by slow solvent modes. The solvent plays a different role in providing the continuum or near continuum of levels required for energy conservation for the individual vibrational channels.

Back electron transfer in the OQD and AFA^{2-} complexes is remarkably slow with the lifetime of the associated RS state reaching 15 μs for the former. These long lifetimes are largely due to the combination of orbital orthogonality and the spin change that accompanies electron transfer. This result has important implications for the design of molecular assemblies for energy conversion and long-term storage of photoproduced redox equivalents. It shows that proper use of electronic effects can greatly influence the lifetimes of electron-transfer transients, even in simple molecular assemblies.

Acknowledgment. This work was supported by the National Science foundation under Grant No. CHE-9705724 to T.J.M.

Supporting Information Available: Supplementary Table 1, with atomic positional parameters for *fac*-[(4,4′-^{t}Bu$_2$bpy)-Re(CO)$_3$(ONQ)]. Supplementary Figure 1, with time-resolved nanosecond transient absorption difference spectra of *fac*-[(4,4′-^{t}Bu$_2$bpy)Re(CO)$_3$(ONQ)]. Supplementary Figure 2, with time-resolved nanosecond transient absorption difference spectra of *fac*-[(4,4′-Me$_2$bpy)Re(CO)$_3$]$_2$(AFA). This material is available free of charge via the Internet at http://pubs.acs.org.

References and Notes

(1) Omberg, K. M.; Chen, P. Y.; Meyer, T. J. *Spectroscopic Determination of Electron-Transfer Barriers and Rate Constants*; Omberg, K. M., Chen, P. Y., Meyer, T. J., Eds.; John Wiley & Sons: New York, 1999; Vol. 106.
(2) Kubo, R.; Toyazara, Y. *Prog. Theor. Phys.* **1955**, *13*, 160.
(3) Lax, M.; Burstein, E. *Phys. Rev.* **1955**, *100*, 592.
(4) Hush, N. S. *Coord. Chem. Rev.* **1985**, *64*, 135−157.
(5) Hush, N. S. *Electrochim. Acta* **1968**, *13*, 1005.
(6) Hush, N. S. *Prog. Inorg. Chem.* **1967**, *8*, 391.
(7) Englman, R.; Jortner, J. *Mol. Phys.* **1970**, *18*, 145−164.
(8) Bixon, M.; Jortner, J. *J. Chem. Phys.* **1968**, *48*, 715−726.
(9) Ulstrup, J.; Jortner, J. *J. Chem. Phys.* **1975**, *63*, 4358.
(10) Newton, M. D.; Sutin, N. *Annu. Rev. Phys. Chem.* **1984**, *35*, 437−480.
(11) Marcus, R. A.; Sutin, N. *Biochim. Biophys. Acta* **1985**, *811*, 265−322.
(12) Siders, P.; Marcus, R. A. *J. Am. Chem. Soc.* **1981**, *103*, 748.
(13) Marcus, R. A. *J. Phys. Chem.* **1989**, *93*, 3078.
(14) Myers, A. B. *Chem. Rev.* **1996**, *96*, 911.
(15) Caspar, J. V.; Sullivan, B. P.; Kober, E. M.; Meyer, T. J. *Chem. Phys. Lett.* **1982**, *91*, 91−95.
(16) Kober, E. M.; Caspar, J. V.; Lumpkin, R. S.; Meyer, T. J. *J. Phys. Chem.* **1986**, *90*, 3722−3734.
(17) Barqawi, K. R.; Murtaza, Z.; Meyer, T. J. *J. Phys. Chem.* **1991**, *95*, 47−50.
(18) Worl, L. A.; Strouse, G. F.; Younathan, J. N.; Baxter, S. M.; Meyer, T. J. *J. Am. Chem. Soc.* **1990**, *112*, 7571−7578.
(19) Bixon, M.; Jortner, J.; Cortes, J.; Heitele, J.; Michel-Beyerle, M. E. *J. Phys. Chem.* **1994**, *98*, 1289.
(20) Gould, S.; Gray, K. H.; Linton, R. W.; Meyer, T. J. *Inorg. Chem.* **1992**, *31*, 5521−5525.
(21) Gould, I. R.; Young, R. H.; Moody, R. E.; Farid, S. *J. Phys. Chem.* **1991**, *95*, 2068.
(22) Gould, I. R.; Young, R. H.; Mueller, L. J.; Albrecht, A. C.; Farid, S. *J. Am. Chem. Soc.* **1994**, *116*, 3147.
(23) Gould, I. R.; Young, R. H.; Mueller, L. J.; Albrecht, A. C.; Farid, S. *J. Am. Chem. Soc.* **1994**, *116*, 8188.
(24) Bixon, M.; Jortner, J.; Verhoeven, J. W. *J. Am. Chem. Soc.* **1994**, *116*, 7349.
(25) Gould, I. R.; Farid, S. *Acc. Chem. Res.* **1996**, *29*, 522−528.
(26) Gust, D.; Moore, T. A.; Moore, A. L. *Science* **1990**, *249*, 199.
(27) Nelsen, S. F.; Ismagilov, R. F.; Trieber, D. A., II *Science* **1997**, *278*, 846−849.
(28) Nelson, S. F.; Ramin, M. T.; Wolff, J. J.; Powell, J. J. *J. Am. Chem. Soc.* **1997**, *119*, 6863.
(29) Derr, D. L.; Elliott, C. M. *J. Chem. Phys. A* **1999**, *103*, 7880.
(30) Moore, A. L.; Moore, T. A.; Macpherson, A. N. *Pure and Appl. Chem.* **1997**, *69*, 2111.
(31) Gust, D.; Moore, T. A. *Science* **1989**, *244*, 35−41.
(32) Wasielewski, M. R. *Chem. Rev.* **1992**, *92*, 435.
(33) Wasielewski, M. R.; Gaines, G. L., III.; O'Neill, M. P.; Svec, W. A.; Niemcayk, M. P. *J. Am. Chem. Soc.* **1990**, *112*, 4559.
(34) Waslielewski, M. R.; Niemczyk, M. P.; Svec, W.; Pewitt, E. B. *J. Am. Chem. Soc.* **1985**, *107*, 5662.
(35) Schanze, K. S.; MacQueen, D. B.; Perkins, T. A.; Cabana, L. A. *Coord. Chem. Rev.* **1993**, *122*, 63.
(36) Schanze, K. S.; Walters, K. A. *Photoinduced Electron Transfer in Metal-Organic Dyads*; Schanze, K. S., Walters, K. A., Eds.; Marcel Delcher: New York, 1998; Vol. 2.
(37) Balzani, V.; Scandola, F. *Supramolecular Photochemistry.*; Ellis Horwood: New York, 1991.
(38) Chen, P.; Duesing, R.; Graff, D. K.; Meyer, T. J. *J. Phys. Chem.* **1991**, *95*, 5850−5858.
(39) Meyer, T. J. *Acc. Chem. Res.* **1989**, *22*, 163−170.
(40) Petersen, J. D.; Murphy, W. R.; Sahai, R.; Brewer, K. J.; Ruminski, R. R. *Coord. Chem. Rev.* **1985**, *64*, 261−272.
(41) Sullivan, B. P.; Abruña, H. O.; Finklea, D. J.; Salmon, D. J.; Nagle, J. K.; Meyer, T. J.; Sprintschnik, H. *Chem. Phys. Lett.* **1978**, *58*, 389.
(42) Mecklenburg, S. L.; McCafferty, D. G.; Schoonover, J. R.; Peek, B. M.; Erickson, B. W.; Meyer, T. J. *Inorg. Chem.* **1994**, *33*, 2974−2983.
(43) Opperman, K. A.; Mecklenburg, S. L.; Meyer, T. J. *Inorg. Chem.* **1994**, *33*, 5295−5301.

(44) Goulle, V.; Harriman, A.; Lehn, J.-M. *J. Chem. Soc., Chem. Commun.* **1993**, 1034.
(45) Berthon, R. A.; Colbran, S. B.; Moran, G. M. *Inorg. Chim. Acta* **1993**, *204*, 3.
(46) Deisenhofer, J.; Epp, O.; Miki, K.; Huber, R.; Michel, H. *J. Mol. Biol.* **1984**, *180*, 385−398.
(47) Claude, J. P.; Williams, D. S.; Meyer, T. J. *J. Am. Chem. Soc.* **1996**, *118*, 9782.
(48) Hadda, T. B.; LeBozec, H. *Polyhedron* **1988**, *7*, 575.
(49) Worl, L. A.; Duesing, R.; Chem, P.; Della Ciana, L.; Meyer, T. J. *J. Chem. Soc., Dalton Trans.* **1991**, 849−858.
(50) Gabe, E. J.; LePage, Y.; Charland, J.-P.; Lee, F. L.; White, P. S. *J. Appl. Crystallogr.* **1989**, *22*, 384.
(51) Omberg, K. M.; Schoonover, J. R.; Treadway, J. A.; Leasure, R. M.; Dyer, R. B.; Meyer, T. J. *J. Am. Chem. Soc.* **1997**, *119*, 7013−7018.
(52) Burie, J.-R.; Boussac, A.; Boullais, C.; Berger, G.; Mattioli, T.; Mioskowski, C.; Nabedryk, E.; Breton, J. *J. Phys. Chem.* **1995**, *99*, 4059.
(53) Omberg, K. M.; Dattelbaum, D. M.; Schoonover, J. R.; Meyer, T. J. *Inorg. Chem.*, submitted.
(54) Striplin, D. R.; Crosby, G. A. *Chem. Phys. Lett.* **1994**, *221*, 426−430.
(55) Danielson, K.; Elliott, C. M.; Merkert, J. W.; Meyer, T. J. *J. Am. Chem. Soc.* **1987**, *109*, 2519.
(56) Watanabe, T.; Honda, K. *J. Phys. Chem.* **1982**, *86*, 2617.
(57) Elliott, C. M.; Freitag, R. A.; Blaney, D. D. *J. Am. Chem. Soc.* **1985**, *107*, 4647−4655.
(58) Nakayama, T.; Ushida, K.; Hamanoue, K.; Wahio, M.; Tagawa, S.; Tabata, Y. *J. Chem. Soc., Faraday Trans. 1* **1990**, *86*, 2617.
(59) Chen, P.; Danielson, E.; Meyer, T. J. *J. Phys. Chem.* **1988**, *92*, 3708−3711.
(60) Omberg, K. M.; Schoonover, J. R.; Meyer, T. J. *J. Phys. Chem.* **1997**, *101*, 9531.
(61) Schoonover, J. R.; Strouse, G. F.; Dyer, R. B.; Bates, W. D.; Chen, P.; Meyer, T. J. *Inorg. Chem.* **1996**, *35*, 273−274.
(62) Rossenaar, B. D.; Stufkens, D. J.; Vlcek, A. J. *Inorg. Chem.* **1996**, *35*, 2902−2909.
(63) Rossenaar, B. D.; George, M. W.; Johnson, F. P. A.; Stufkens, D. J.; Turner, J. J.; Vlcek, A., Jr. *J. Am. Chem. Soc.* **1995**, *117*, 11 582−11 582.
(64) Stufkens, D. J.; Vlcek, A., Jr. *The Spectrum* **1996**, *9*, 2−7.
(65) Chen, P. Y.; Meyer, T. J. *J. Chem. Rev.* **1998**, *98*, 1439.
(66) Mallick, P. K.; Danzer, G. D.; Strommen, D. P.; Kincaid, J. R. *J. Phys. Chem.* **1988**, *92*, 5628.
(67) Strommen, D. P.; Mallick, P. K.; Danzer, G. D.; Lumpkin, R. S.; Kincaid, J. R. *J. Phys. Chem.* **1990**, *94*, 1357.
(68) Strickler, S. J.; Berg, R. A. *J. Chem. Phys.* **1962**, *37*, 814.
(69) Gould, I. R.; Noukakris, D.; Ganez-Jahn, L.; Yound, R. H.; Goodman, J. L.; Farid, S. *Chem. Phys.* **1993**, *126*, 439.
(70) Creutz, C. *Prog. Inorg. Chem.* **1983**, *30*, 1.
(71) Klumpp, T.; Linsemann, M.; Larson, S. L.; Limoges, B. R.; Burssner, D.; Krissinel, E. B.; Elliott, C. M.; Steiner, U. F. *J. Am. Chem. Soc.* **1999**, *121*, 1076.
(72) Tom, G. M.; Creutz, C.; Taube, H. *J. Am. Chem. Soc.* **1974**, *96*, 7828.
(73) Hupp, J. T.; Meyer, T. J. *Inorg. Chem.* **1987**, *26*, 2332.
(74) Creutz, C. *J. Am. Chem. Soc.* **1973**, *95*, 1086.
(75) Creutz, C. *Inorg. Chem.* **1978**, *17*, 3723.
(76) Dubicki, L.; Ferguson, J.; Krausz, E. *J. Am. Chem. Soc.* **1985**, *107*, 179.
(77) Demadis, K.; Hartshorn, C.; Meyer, T. J. *Chem. Rev.* **2001**, *101*, 2655.
(78) Sutin, N.; Creutz, C. *J. Chem. Educ.* **1983**, *60*, 809−814.
(79) Creutz, C.; Newton, M. D.; Sutin, N. *J. Photochem. Photobiol.* **1994**, *82*, 47.
(80) Kestner, N. R.; Logan, J.; Jortner, J. *J. Phys. Chem.* **1974**, *78*, 2148.
(81) Sutin, N.; Creutz, C. *Pure and Appl. Chem.* **1980**, *52*, 2717−2738.
(82) Siebrand, W.; Zagierski, M. Z. *J. Chem. Phys.* **1979**, *71*, 3561.
(83) Barbara, P. F.; Meyer, T. J.; Ratner, M. A. *J. Phys. Chem.* **1996**, *100*, 13 148−13 168.
(84) Lin, C.; Bottcher, W.; Chou, M.; Creutz, C.; Sutin, N. *J. Am. Chem. Soc.* **1976**, *98*, 6536−6544.
(85) Jortner, J. *J. Chem. Phys.* **1976**, *64*, 4860.
(86) Gilch, P.; Pollinger-Dammer, F.; Musewald, C.; Michel-Beyerle, M. E.; Steiner, U. E. *Science* **1998**, *281*, 982.